Research article

Early estimation method of rockburst and large deformation of surrounding rock based on the deep borehole test

Kai Cui [a], Zheng Yang [b],*

[a] *College of Construction Engineering, Sanmenxia Polytechnic, Sanmenxia, Henan, China*
[b] *School of Resources and Safety Engineering, Central South University, Changsha, Hunan, China*

A B S T R A C T

In geotechnical engineering, several major catastrophic accidents occur frequently in areas of high in-situ stress. To study the influence of high in-situ stress on deep mining, the in-situ stress was tested using the hydraulic fracturing method in the mine. Based on the measured data of the initial stress, a comprehensive evaluation of the stress field of the deep surrounding rocks was carried out. Combining the physical and mechanical indexes of the surrounding rocks, field measurements, and theoretical analysis, the Russenes criterion and Turchaninov criterion were applied to evaluate the propensity of rockbursts of hard rocks in the mine area. In addition, the large deformation of the soft rock in the mine was predicted based on the large deformation classification criteria. The results demonstrate that the vertical stress is linearly related to the depth. The horizontal principal stress values tested in all holes except boreholes G and I are approximately linearly distributed with depth. The greater the depth, the greater the propensity for rockburst. For obvious deviation from the maximum horizontal main stress direction of the mining tunnel, the tendency of rockburst during construction is greater. Slight deformation occurs when the tunnel surrounding rock is shallow than 660 m; larger deformation occurs when the burial depth exceeds 660 m. Level-II or level-III deformations may occur near the bottom of holes F, G, and I due to the lower uniaxial compressive strength of the phyllites of these holes.

1. Introduction

As the mining depth of metal mines in China increases, the stress environment of the rocks changes. The mechanical properties of deep rocks are significantly different than those of shallow rocks, resulting in varying degrees of deviation from the experience gained during shallow mineral development when applied to deeper mining [1–3]. Meanwhile, the hazards caused by the complex geological environment at depth are increasing. Therefore, the study of deep rocks and their complex stress environment is of great significance to reveal the causes and effective prevention of geological hazards induced by deep mining.

Rock is a collection of various minerals in nature, which generally contains a large number of defects such as holes, cracks, joints, faults, etc. [4–11]. Thus, the inherent structural characteristics of rock materials are the presence of a large number of defects and multiple components. Rocks are characterized by discontinuity, non-uniformity, anisotropy, and inelasticity. In shallow environments, the above-mentioned features or defects of rocks are not obvious. While in deep and complex conditions, the defects of rocks are often amplified, which triggers a series of responses. The damage patterns and characteristics of rocks under high initial stresses (in-situ

---

stress) have changed considerably. Rock failure caused by high stresses has been extensively studied in the past [12–20]. For instance, He et al. [3] conducted a single-sided dynamic unloading test on sedimentary limestone samples under true triaxial conditions. Chen et al. [21] investigated the effect of confining pressure and unloading rate on crack propagation characteristics. The results showed that a larger unloading rate caused a larger crack propagation rate, which may trigger rock bursts. Rockbursts are sudden dynamic hazards induced by rock deformation and fracture [22,23]. Zhu et al. [24] conducted laboratory experiments using a true triaxial rockburst system to investigate the effect of a hyper-stress state on rockburst in deep underground coal mining. The experimental results showed that the coal samples were more prone to deformation and damage under triaxial unloading compared to triaxial loading. In addition, there have been many field investigations of geotechnical hazards besides laboratory studies. For example, Xu et al. [25] reported strain bursting in a considerable section of the deep tunnel excavation in the Jinping II hydropower project in China. Feng et al. [26] studied the damage mechanism of rock spalling in the same project and found that the thickness of the cleavage plate increased inward from the sidewall. Previous work on the physical and mechanical properties of rocks under high stress has greatly enriched our understanding. However, there are fewer systematic field studies related to high initial stresses.

To study the influence of high in-situ stress on deep mining, this paper takes a metal mine in China as an example. The in-situ stress was tested using the hydraulic fracturing method. Based on the measured data of the initial stress, a comprehensive evaluation of the stress field of the deep surrounding rocks of the mine was carried out. Combining the field measurements and theoretical analysis, Russenes' discriminant method and Turchaninov's discriminant method were applied to evaluate the propensity of rockbursts of hard rocks in the mine area. In addition, based on the large deformation classification criteria, the large deformation of the surrounding rocks in the mine was predicted. The study conducted a comprehensive risk estimation of the mine. The results provide a beneficial theoretical basis and guidance for the prevention and control of hazards induced by high in-situ stress.

2. Regional geological out

The mine area is a hilly low-mountain landscape with slope angles of 10°–35° due to weathering and rain erosion and forms dendritic gullies, pre-mountain valleys, and low-middle mountains. The terrain of the mine area is high in the northeast and low in the southwest and flows into the river from the northeast to the southwest. The highest peak in the mine area is 307.63 m above sea level, and the maximum relative height difference of the terrain is 227.63 m. The mine area is 3.4 km long from north to south and 2.8 km wide from east to west, with an area of about 9.0 km^2.

The exposed strata in the area include the Middle Paleozoic Shuangqiao Mountain Group (Pt2sh), the Upper Paleozoic Mountaineering Group (Pt3d) and the Earthquake Series (Z), the Paleozoic Cambrian (Є), the Mesozoic Jurassic (J) and Cretaceous (K), as well as the Cenozoic Quaternary (Q). With the ductile shear zone as the boundary, the shallow metamorphic system of the Mountain Group is exposed in a large area on the northwest side. Its exposed area accounts for about 70% of the whole area. On the southeast side of the shear zone, the Mountain Group, the Aurora Series, the Cambrian Series, the Jurassic Series, and the Cretaceous Series are sporadically distributed in the central west and southeast. The Fourth Series is distributed along the river valleys and small basins in the ravines.
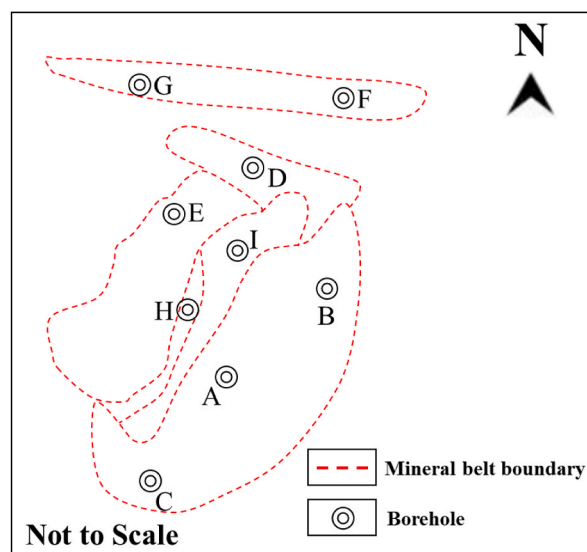

Fig. 1. Schematic layout of the borehole.

3. On-site in-situ experiments

3.1. Borehole description

The initial stress is the basic force that triggers many rock hazards. It is the prerequisite for the stability analysis of the surrounding rock. For the initial stress test, 9 boreholes were selected in the mine. The locations of the boreholes are shown in Fig. 1. A total of 90 actual measurements were obtained from the initial stress tests. The details of each borehole are shown in Table 1.

3.2. Principles and methods of initial stress testing

Hydraulic fracturing is one of the recommended methods for determining rock stresses promulgated by the Test Methods Committee of the International Society of Rock Mechanics in 1987 and 2003 [27]. Compared to the other 3 recommended measurement methods, hydraulic fracturing has the following outstanding advantages: (1) superior measurement depth; (2) no need for rock elastic parameters (3) a wide range of rock wall forces (4) simple operation and short test cycle. Therefore, hydraulic fracturing is widely used in water conservancy and hydropower, transportation, mining, as well as other industries. The principle of hydraulic fracturing is that a pair of expandable rubber packers are used to seal a section of the borehole at a predetermined test depth, and then the fluid is pumped to apply pressure to the section. The in-situ stress is calculated from the pressure characteristic values of the fracturing process curve. Fig. 2a and b show the schematic diagram of the test equipment for the magnitude and direction of the principal stress of the hydraulic fracturing method.

The following assumptions are made for in-situ stress testing using the hydraulic fracturing method: 1) the surrounding rock is a linear, homogeneous, and isotropic elastomer; 2) the borehole axis is parallel to one of the principal stresses; 3) the pressurization rate is fast enough to neglect the fluid penetrating the rock; 4) the pore water pressure remains essentially constant; 5) the fracture begins at the location of the minimum tangential stress in the borehole wall and extends in a direction perpendicular to the minimum principal stress; 6) the normal stress at the fracture surface is equal to the closure pressure. In addition, the vertical stress σ_V is equal to the self-gravity pressure of the overlying rock when the borehole is vertical, as shown in Fig. 2c. The secondary stress state near the hole when the infinite plane containing the circular hole is subjected to the two-way stresses σ_A and σ_B ($\sigma_A > \sigma_B$) is given by Eq. (1):

$$
\begin{aligned}
\sigma'_\theta &= \frac{\sigma_A + \sigma_B}{2}\left(1 + \frac{a^2}{r^2}\right) - \frac{\sigma_A - \sigma_B}{2}\left(1 + \frac{3a^4}{r^4}\right)\cos 2\theta \\
\sigma'_r &= \frac{\sigma_A + \sigma_B}{2}\left(1 - \frac{a^2}{r^2}\right) + \frac{\sigma_A - \sigma_B}{2}\left(1 + \frac{3a^4}{r^4} - \frac{4a^2}{r^2}\right)\cos 2\theta \\
\tau'_{r\theta} &= -\frac{\sigma_A - \sigma_B}{2}\left(1 - \frac{3a^4}{r^4} + \frac{2a^2}{r^2}\right)\sin 2\theta
\end{aligned}
\tag{1}
$$

where a is the radius of the borehole; r is the radial distance; θ is the angle between the pole diameter and axis; σ'_r, σ'_θ, and $\tau'_{r\theta}$ are the radial stress, tangential stress, and shear stress, respectively; σ_A and σ_B are the maximum and minimum principal stresses in the cross-section of the borehole, respectively. The stress state around the hole ($r = a$) is given by Eq. (2):

$$
\begin{aligned}
\sigma'_\theta &= (\sigma_A + \sigma_B) - 2(\sigma_A - \sigma_B)\cos 2\theta \\
\sigma'_r &= 0 \\
\tau'_{r\theta} &= 0
\end{aligned}
\tag{2}
$$

The additional stress generated by the hydraulic pressure P_w during the hydraulic fracturing test is given by Eq. (3):

$$
\begin{aligned}
\sigma''_\theta &= -P_w\frac{a^2}{r^2} \\
\sigma''_r &= P_w\frac{a^2}{r^2}
\end{aligned}
\tag{3}
$$

Table 1
Details of each borehole.

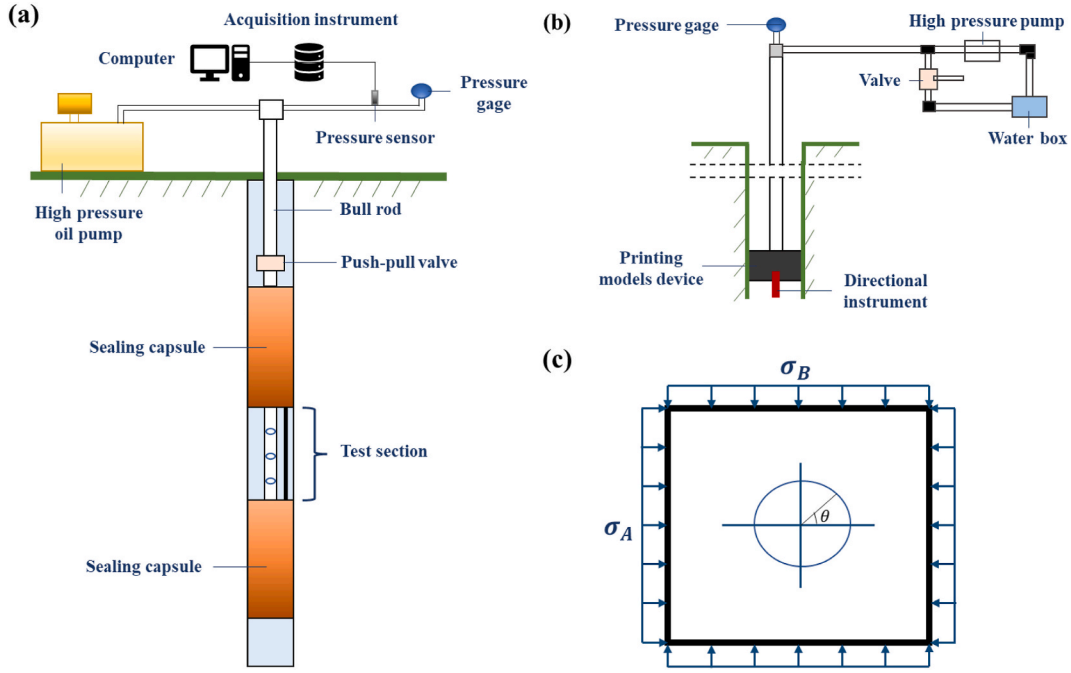| Number	Depth/m	Segment of fracturing
A	465	10
B	484	10
C	337	10
D	620	12
E	640	10
F	372	10
G	310	8
H	634	10
I	505	10

Fig. 2. Principle diagram of hydraulic fracturing. (a) Test equipment for primary stress magnitude; (b) Test equipment for horizontal principal stress direction; (c) Stress state of the infinite plane containing a circular hole.

The additional stress around the hole ($r = a$) is described by Eq. (4):

$$\sigma''_\theta = -P_w$$
$$\sigma''_r = P_w$$

(4)

The stress on the rock wall of the drill hole is:

$$\sigma_\theta = \sigma'_\theta + \sigma''_\theta = (\sigma_A + \sigma_B) - 2(\sigma_A - \sigma_B)\cos 2\theta - P_W$$

(5)

The fractures occur at the site of maximum tensile stress in the borehole wall. Therefore, it is necessary to focus on the area where the minimum stress occurs in the secondary stress field of the surrounding rock. As seen from Eq. (5), the tangential stress is minimum at $\theta = 0$ or $\theta = \pi$ in the borehole wall. Thus, Eq. (6) can be obtained:

$$\sigma_\theta = 3\sigma_B - \sigma_A - P_W$$

(6)

The critical pressure (P_b) for rock fracture is given by Hemmerson, as shown in Eq. (7):

$$P_b - P_0 = \frac{3(\sigma_B - P_0) - (\sigma_A - P_0) + \sigma_t}{K}$$

(7)

where K is the pore permeability elasticity coefficient, which is determined in the test chamber and varies from 1 to 2. P_0 is the pore water pressure. For non-permeable rocks, the value of K is approximately equal to 1, and Eq. (7) can be rewritten as Eq. (8):

$$P_b - P_0 = 3\sigma_B - \sigma_A + \sigma_t - 2P_0$$

(8)

When the borehole is vertical, σ_A and σ_B are the maximum and minimum horizontal principal stresses σ_H and σ_h. Substituting in-situ stress for the effective stress in the above equation yields:

$$P_b = 3\sigma_h - \sigma_H + \sigma_t - P_0$$

(9)

According to the principle that the fracture propagates along the path of least resistance, the instantaneous closing pressure P_s that maintains the fracture opening after closing the pressure pump is equal to the compressive stress in the direction of the vertical rupture surface, i.e., the minimum horizontal principal stress is given by Eq. (10):

$$\sigma_h = P_S$$

(10)

The maximum horizontal principal stress obtained according to Eq. (9) is described by Eq. (11):

$$\sigma_H = 3\sigma_h - P_b - P_0 + \sigma_t$$

(11)

The re-tensioning pressure P_r is:

$$P_r = 3\sigma_h - \sigma_H - P_0 \tag{12}$$

The maximum horizontal principal stress can also be calculated directly using the re-tensioning pressure, as demonstrated in Eq. (13):

$$\sigma_H = 3\sigma_h - P_r - P_0 \tag{13}$$

Comparing Eqs. (9) and (12), the tensile strength of the rock at the hole wall can be approximated by Eq. (14):

$$\sigma_t = P_b - P_r \tag{14}$$

The vertical stress σ_z can be estimated from the weight of the overlying rock as in Eq. (15):

$$\sigma_z = \gamma * H \tag{15}$$

where γ is the rock capacity and H is the thickness of the overlying rock layer. The above is the basic principle and parameters calculation method of in-situ stress measurement by hydraulic fracturing method.

4. Experimental results and discussion

4.1. Evolution of the initial stress

The initial stress measurements were performed on nine boreholes according to the method described above. Typical fracture curves in this experiment are shown in Fig. 3. All test curves are following the general rule of hydraulic fracturing testing. Fig. 4(a–i) plots the variation of maximum horizontal principal stress, minimum horizontal principal stress, and vertical stress with depth. The vertical stress was linearly related to the depth. Moreover, the maximum horizontal principal stress and minimum horizontal principal stress were fitted linearly with depth *H,* and the fitted equations were as follows:

$$\begin{aligned} \sigma_H &= aH + b \\ \sigma_h &= cH + d \end{aligned} \tag{16}$$

where a, b, c, and d are the fitted correlation coefficients in Eq. (16). The corresponding coefficients for each borehole are shown in Table 2. The results show that the horizontal principal stress values tested in all holes except boreholes G and I are approximately linearly distributed with depth. The deviation of the horizontal principal stresses in holes G and I may be attributed to the large local tectonic compression effect. For boreholes B, C, G, and I, the measured stress values are mainly characterized by $\sigma_H > \sigma_h \approx \sigma_z$, dominated by horizontal stress. For boreholes A, D, E, F, and H, the measured stress values are mainly characterized by $\sigma_H \approx \sigma_z > \sigma_h$, dominated together with self-weight stress.

In addition, the stress orientation was also measured. The maximum horizontal principal stress direction in borehole A was from N23°E to N31°E; the maximum horizontal principal stress direction in borehole B was from N18°E to N26°E; the maximum horizontal principal stress direction in borehole C was from N19°E to N32°E; the maximum horizontal principal stress direction in borehole D was from N12° to 28°E; the maximum horizontal principal stress direction in borehole E was from N20°E to The maximum horizontal principal stress direction in borehole F is from N24°E to N36°E, the maximum horizontal principal stress direction in borehole G is from N31°E to N37°E, the maximum horizontal principal stress direction in borehole H is from N18° to 28°E, and the maximum horizontal principal stress direction in the borehole I is from N27°E to N35°E. The maximum horizontal principal stress direction in all the measured boreholes is from NNE to NE, which indicates that the maximum horizontal principal stress direction in the present day in all the measured boreholes is NNE to NE direction, indicating that the present-day tectonic stress field in the project area is dominated by NNE to NE direction extrusion.

4.2. Evaluation and calculation of the stress field of the surrounding rock

The test results of ground stresses of the above nine holes show that the maximum horizontal principal stress is generally in the NNE
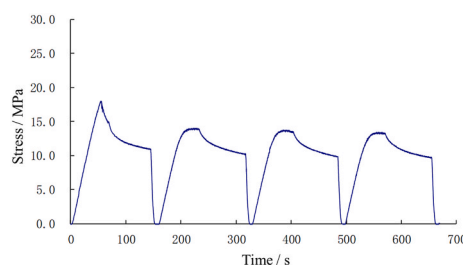

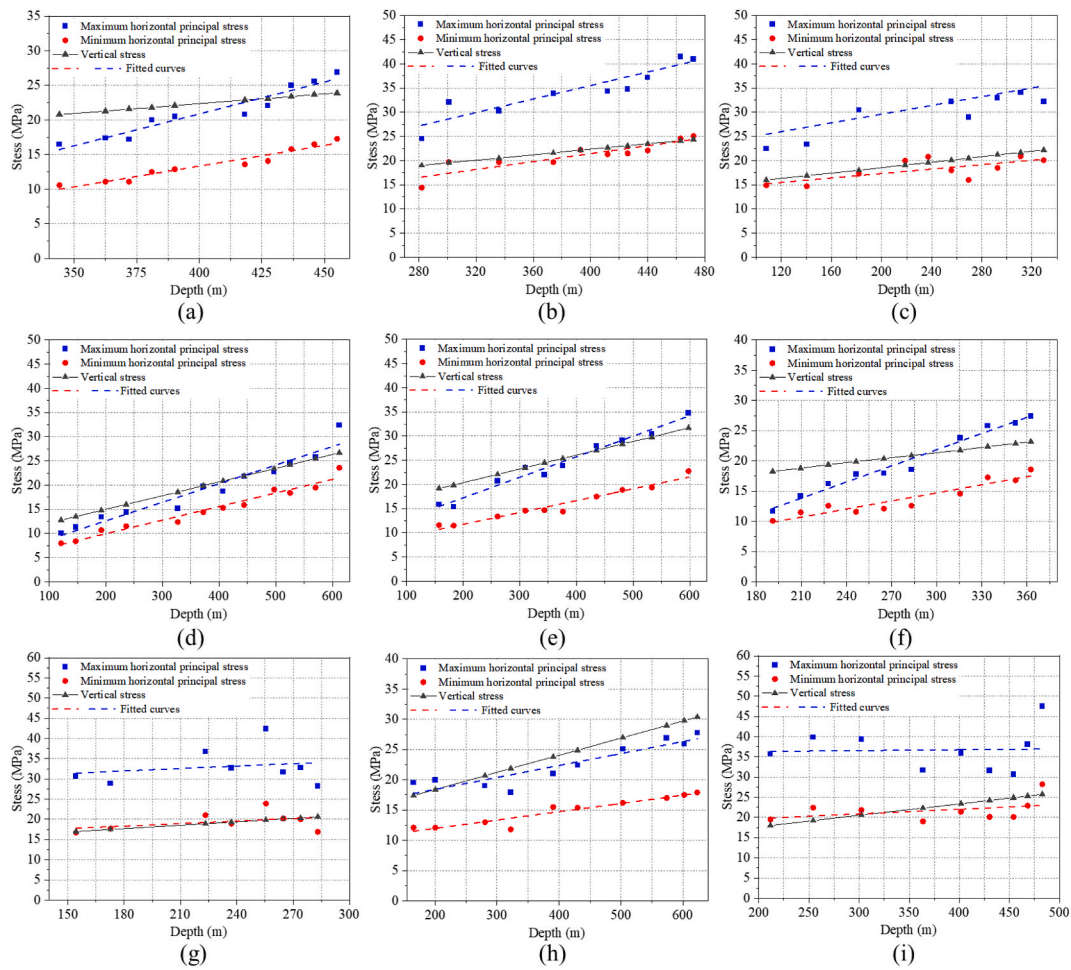**Fig. 3.** Typical fracturing curves for hydraulic fracturing.

Fig. 4. Variation of maximum horizontal principal stress, minimum horizontal principal stress, and lead stress with depth. (a) Borehole A, (b) Borehole B, (c) Borehole C, (d) Borehole D, (e) Borehole E, (f) Borehole F, (g) Borehole G, (h) Borehole H, (i) Borehole I.

Table 2
Corresponding coefficients for each borehole.

Number	a	b	c	d
A	0.092	−15.9	0.059	−10.6
B	0.070	7.6	0.041	5.1
C	0.045	20.57	0.022	12.74
D	0.038	4.93	0.028	4.35
E	0.042	8.76	0.024	6.86
F	0.089	−4.87	0.045	1.35
G	0.020	28.37	0.020	14.59
H	0.019	14.44	0.014	9.22
I	0.002	35.92	0.011	17.39

to NE direction (average NE27°). The in-situ stress values vary greatly with different boreholes. Specifically, the maximum horizontal principal stresses in boreholes A, D, E, F, and H are comparable to the vertical stresses (the lateral pressure coefficient is about 1.0), while the maximum horizontal principal stresses in boreholes B, C, G and I are significantly higher than the vertical stresses (the lateral pressure coefficients are as high as 1.5 or more). Thus, based on the characteristics of the in-situ measurement results, the distribution law of the local stress field at the locations of different boreholes was studied. For the boreholes A, D, E, F, H, and their neighbors, the expressions for the in-situ stress field are as follows:

$$\begin{cases} \sigma_H = 1.0\gamma H \\ \sigma_h = 0.7\gamma H \\ \sigma_Z = \gamma H \end{cases}$$

(17)

where H is the burial depth of the surrounding rock. For the boreholes B, C, G, I, and their adjacent areas, the expressions for the in-situ stress field are as follows:

$$\begin{cases} \sigma_H = 1.6\gamma H \\ \sigma_h = 1.0\gamma H \\ \sigma_Z = \gamma H \end{cases}$$

(18)

According to the above expressions for the in-situ stress field and the Specification for Geological Survey of Hydroelectric Power Engineering (GB50287-2016), the burial depth distribution range of high and extremely high stresses near each borehole can be derived, as shown in Table 3. It is well known that the graded characteristics of the ground stress values are related to the engineering geological conditions near the boreholes. As several boreholes with relatively concentrated vein distribution, the maximum horizontal principal stresses measured in boreholes A, D, E, F, and H are comparable to the vertical stresses. It is mainly since the boreholes in this area expose many veins and the rock integrity is relatively poor, resulting in relatively low in-situ stress. The burial depth from 880 m to 1760 m is a high-stress level. The burial depth of over 1760 m is an extremely high-stress level.

The maximum horizontal principal stresses measured in holes C, B, G, and I far from the concentrated distribution of veins are greater than the vertical stresses. The stress values obtained from the tests are relatively high due to the fewer veins exposed and the relatively excellent rock integrity away from the concentrated vein distribution area. The stress level is high at the burial depth of 550 m–1100 m and extremely high at the burial depth of more than 1100 m.

It can be seen that the distribution of the in-situ stress field in the mine area is complex, not only by the local tectonic influence of the vein assignment but also by the complex lithological distribution of the mine area. In addition, the mine is located in a deep large fracture zone with super crystal characteristics. The local characteristics of the in-situ stress field vary greatly, which is confirmed by the results of this study.

To predict the rock wall deformation and rockburst after the excavation of the roadway during the deep mining process in the future, the maximum tangential stress on the cross-section of the roadway is required to be calculated. Fig. 5a shows the horizontal stress of the rock in the roadway axis when the tunnel is not excavated. σ_H and σ_h are the maximum and minimum horizontal principal stresses respectively, which can be obtained from the fitted lines in the previous section. σ_H' and σ_L are the horizontal stresses perpendicular and parallel to the roadway axis, respectively. α is the angle between σ_H and σ_H'. θ is the angle between the direction of σ_H and the axial direction of the roadway. σ_H' and σ_L are calculated by Eq. (19).

$$\sigma_H' = \frac{1}{2}(\sigma_H + \sigma_h) + \frac{1}{2}(\sigma_H - \sigma_h)\cos 2\alpha$$

$$\sigma_L = \frac{1}{2}(\sigma_H + \sigma_h) - \frac{1}{2}(\sigma_H - \sigma_h)\cos 2a$$

(19)

The tangential stresses on the cross-sectional surface of the roadway were estimated based on the circular hole. The stress at the top of the tunnel and the midpoint of the side wall is shown in Fig. 5b. The stresses are calculated as in Eq. (20).

$$(\sigma_\theta)_{top} = 3\sigma_H' - \sigma_Z$$

$$(\sigma_\theta)_{side} = 3\sigma_Z - \sigma_H'$$

(20)

where $(\sigma_\theta)_{top}$ and $(\sigma_\theta)_{side}$ are the tangential stresses at the top of the tunnel and the midpoint of the side wall, respectively. The maximum value of the tangential stress in the cavity wall is given by Eq. (21):

$$\sigma_{\theta\ max} = \begin{cases} (\sigma_\theta)_{top} = 3\sigma_H' - \sigma_z & (\sigma_H' \geq \sigma_z) \\ (\sigma_\theta)_{side} = 3\sigma_z - \sigma_H' & (\sigma_H' < \sigma_z) \end{cases}$$

(21)

Table 3
Stress classification for different burial depths near the borehole.

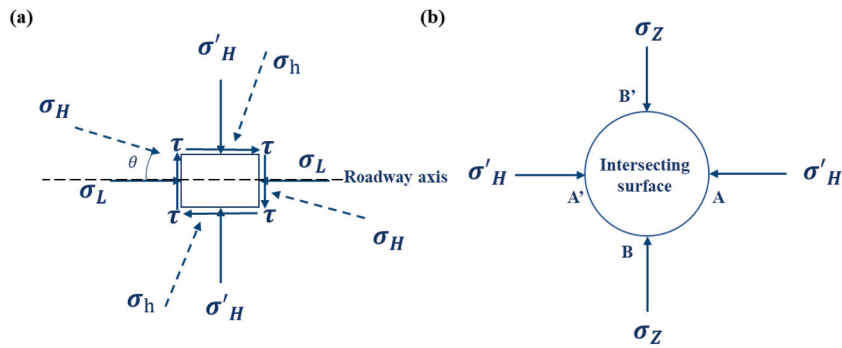| Number	High stresses	Extremely high stresses
A	880 m<H < 1760 m	H > 1760 m
B	550 m<H < 1100 m	H > 1100 m
C	550 m<H < 1100 m	H > 1100 m
D	880 m<H < 1760 m	H > 1760 m
E	880 m<H < 1760 m	H > 1760 m
F	880 m<H < 1760 m	H > 1760 m
G	550 m<H < 1100 m	H > 1100 m
H	880 m<H < 1760 m	H > 1760 m
I	550 m<H < 1100 m	H > 1100 m

Fig. 5. (a) Horizontal stress of the rock in the roadway axis; (b) Stress in the cross section of the roadway.

Based on the above method, the in-situ stress and the maximum tangential stress at the maximum burial depth can be obtained for each borehole, respectively, as shown in Table 4.

4.3. Rockburst prediction

Rockburst is a dynamic destabilization geohazard caused by the sudden release of elastic strain energy of the rock body under the action of high initial stress and excavation disturbance [28,29]. The prediction and evaluation of rockburst are critical to safe mining. Rock explosion factors include internal and external factors. Internal factors are mainly high initial stress, rock structure, performance, as well as geological structure. External factors are mainly hydrogeological conditions, excavation, construction factors, and stress wave shallow epidermal transformation. Generally, the rockburst only happens for hard rock [30]. High initial stress is the source of energy for the occurrence of rockburst. Based on the initial stresses obtained from the above calculations, the generally accepted Russenes criterion [31,32] and Turchaninov criterion [33,34] were used for the comprehensive evaluation of rockburst.

The Russenes criterion establishes a rockburst intensity relationship based on the relationship between the maximum tangential stress in the roadway and the point load strength of the rock. The point load strength converted to the uniaxial compressive strength R_c of the rock. The discriminant equation is as follows.

The Turchaninov criterion was obtained based on the experience of mine construction on Kola Island [35]. Rockburst tendency is determined by the ratio of the sum of tangential stress σ_θ and axial stress σ_L in the roadway to the uniaxial compressive strength R_c of the rock, as shown below.

The analysis is carried out for the intact hard rock in the maximum horizontal main stress direction of the roadway where rock explosion may occur. Referring to the test results and engineering experience, the uniaxial compressive strength of rock R_c is taken as 50.0 MPa. Based on Tables 5 and 6, rockburst prediction results can be obtained, as shown in Tables 7, 8, and Fig. 6. The results show a positive correlation between depth and the propensity for rockburst. It should be noted that the propensity for rockburst is higher in areas with concentrated vein distribution than in areas far from the concentrated vein distribution. Meanwhile, for obvious deviation from the direction of the maximum horizontal main stress, there is a greater possibility of rock explosion. Therefore, it is necessary to take safety precautions in roadway excavation.

4.4. Soft rock deformation prediction

For deep mining, the deformation of soft rocks under high stress is not negligible. The large deformation occurring in the roadway can be divided into the following two main types: (1) Expansion-type large deformation: large deformation caused by the expansion effect of the swelling surrounding rock composed of clay minerals after absorbing water. (2) Extrusion-type large deformation: plastic

Table 4
The in-situ stress and the maximum tangential stress at the maximum burial depth.

Number	Depth (m)	Geostress (MPa)			σ'_H (MPa)	σ_L (MPa)	$\sigma_{\theta\max}$ (MPa)
		σ_H	σ_h	σ_Z			
A	465.4	26.7	17.2	24.2	17.2	26.7	55.5
B	484.3	41.5	25.0	24.7	25.0	41.5	50.1
C	337.7	34.6	19.4	22.5	22.5	34.6	48.0
D	620.1	29.1	21.8	26.9	21.8	29.1	26.9
E	640.7	35.7	22.9	32.9	22.9	35.7	75.7
F	372.0	27.9	17.7	23.4	27.9	17.7	52.5
G	310.0	34.6	21.1	21.4	34.6	21.1	43.1
H	634.5	27.1	18.1	30.7	27.1	18.1	74.0
I	505.05	43.8	26	26.3	43.8	26.0	52.9

Note: It is assumed that the roadway is parallel to the maximum horizontal principal stress.

Table 5
Rockburst evaluation using Russenes criterion.

Classification of rockburst	σ_θ/R_c
No rockburst	$\sigma_\theta/R_c < 0.2$
Slight rockburst	$0.20 \leq \sigma_\theta/R_c < 0.3$
Medium rockburst	$0.30 \leq \sigma_\theta/R_c < 0.5$
Strong rockburst	$\sigma_\theta/R_c \geq 0.55$

Table 6
Rockburst evaluation using Turchaninov criterion.

Classification of rockburst	$(\sigma_\theta + \sigma_L)/R_c$
No rockburst	$(\sigma_\theta + \sigma_L)/R_c \leq 0.3$
Slight rockburst	$0.3 < (\sigma_\theta + \sigma_L)/R_c \leq 0.5$
Medium rockburst	$0.5 < (\sigma_\theta + \sigma_L)/R_c \leq 0.8$
Strong rockburst	$(\sigma_\theta + \sigma_L)/R_c > 0.8$

Table 7
Rockburst prediction results (Borehole A, D, E, F, and H).

Russenes criterion			Turchaninov criterion		
Classification of rockburst	σ_θ/R_c	$H\ (m)$	Classification of rockburst	$(\sigma_\theta + \sigma_L)/R_c$	$H\ (m)$
No rockburst	<0.2	<150	No rockburst	≤0.3	≤170
Slight rockburst	(0.2,0.3)	(150,230)	Slight rockburst	(0.3,0.5)	(170,270)
Medium rockburst	(0.3,0.55)	(230,420)	Medium rockburst	(0.5,0.8)	(270,430)
Strong rockburst	≥0.55	≥420	Strong rockburst	>0.8	>430

Table 8
Rockburst prediction results (Borehole C, B, G, and I).

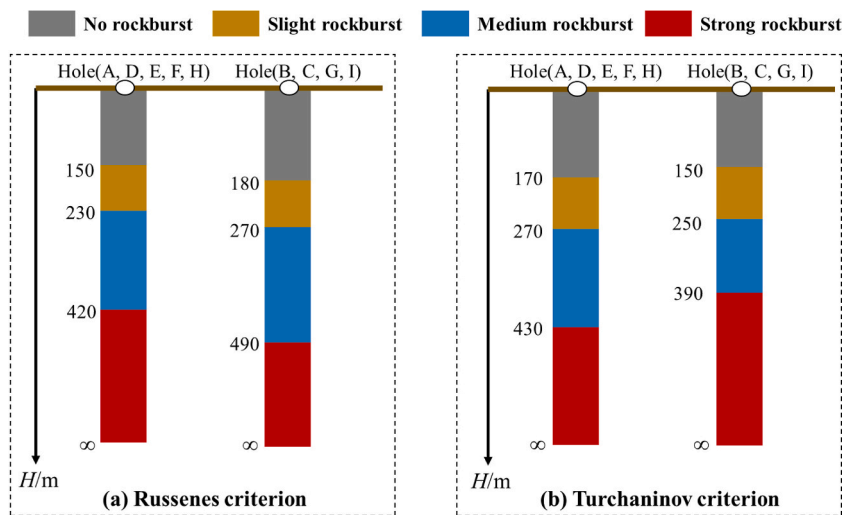| Russenes criterion			Turchaninov criterion		
Classification of rockburst	σ_θ/R_c	$H\ (m)$	Classification of rockburst	$(\sigma_\theta + \sigma_L)/R_c$	$H\ (m)$
No rockburst	<0.2	<180	No rockburst	≤0.3	≤150
Slight rockburst	(0.2,0.3)	(180,270)	Slight rockburst	(0.3,0.5)	(150,250)
Medium rockburst	(0.3,0.55)	(270,490)	Medium rockburst	(0.5,0.8)	(250,390)
Strong rockburst	≥0.55	≥490	Strong rockburst	>0.8	>390

Fig. 6. Rockburst prediction results using (a) Russenes criterion and (b) Turchaninov criterion.

(flow) large deformation formed by the extrusion of soft surrounding rocks under high stress. Its convergence time takes tens of days for short ones and hundreds of days for long ones. The general deformation can reach more than tens of centimeters.

In this study, based on the large deformation grading standard of domestic large soft rock roadway, the characteristics of this mine, physical and mechanical indexes of the surrounding rock, field measurement, and theoretical analysis results, the following comprehensive index determination method is proposed to determine the large deformation grading, as shown in Fig. 7.

The phyllite is the main component of the soft surrounding rock of the roadway. The saturated uniaxial compressive strength of 15 MPa was obtained through field sampling. The excavation depth of the mine generally exceeds 330 m. Based on Eqs. (17) and (18), the strength stress R_c/σ_{max} is 1.0–0.5 in the range of 330 m–660 m. Following the strength-stress ratio criterion, slight deformation occurs when the tunnel surrounding rock is shallow than 660 m; larger deformation occurs when the burial depth exceeds 660 m. It should be noted that level-II or level-III deformations may occur near the bottom of holes F, G and I due to the lower uniaxial compressive strength of the phyllites of these holes. For the surrounding rock with deformation, it is recommended to maintain the roadway stability by adopting a comprehensive control method in stages, i.e. allowing the surrounding rock deformation, releasing the ground stress, reducing the support pressure, and restraining the surrounding rock relaxation and excessive deformation. Specific measures include: 1) choosing a reasonable section shape; 2) leaving enough reserved deformation; 3) over-supporting with short anchor pipes; 4) reinforcing the surrounding rock with medium-length system anchors and a small number of reinforcement anchors; 5) multiple supports; 6) appropriately increasing the lining stiffness; 7) appropriately applying secondary lining in advance.

5. Conclusion

The initial stress in the mine was tested using the hydraulic fracturing method. Based on the measured data of the initial stress, a comprehensive evaluation of the stress field of the surrounding rocks of the mine was carried out. Combining the physical and mechanical indexes of the surrounding rocks, field measurements, and theoretical analysis, the Russenes criterion and Turchaninov criterion were applied to evaluate the propensity of rock bursts of hard rocks in the mine area. In addition, based on the large deformation classification criteria, the large deformation of the soft rock surrounding rocks in the mine was predicted. The following conclusions were obtained.

(1) The vertical stress was linearly related to the depth. The horizontal principal stress values tested in all holes except boreholes G and I are approximately linearly distributed with depth. The deviation of the horizontal principal stresses in holes G and I may be attributed to the large local tectonic compression effect.

(2) The distribution of the stress field in this mine is complex, not only influenced by the local tectonics of the vein deposit but also related to the complex lithological distribution of the mine. In addition, the mine is located in a deep large fracture zone with super crystal characteristics. The local characteristics of the stress field vary greatly, which is confirmed by the results of this test.

(3) The greater the depth, the greater the propensity for rockburst. For obvious deviation from the maximum horizontal main stress direction of the mining tunnel, the tendency of rockburst during construction is greater.

(4) Slight deformation occurs when the tunnel surrounding rock is shallow than 660 m; larger deformation occurs when the burial depth exceeds 660 m. Level-II or level-III deformations may occur near the bottom of holes F, G and I due to the lower uniaxial compressive strength of the phyllites of these holes.
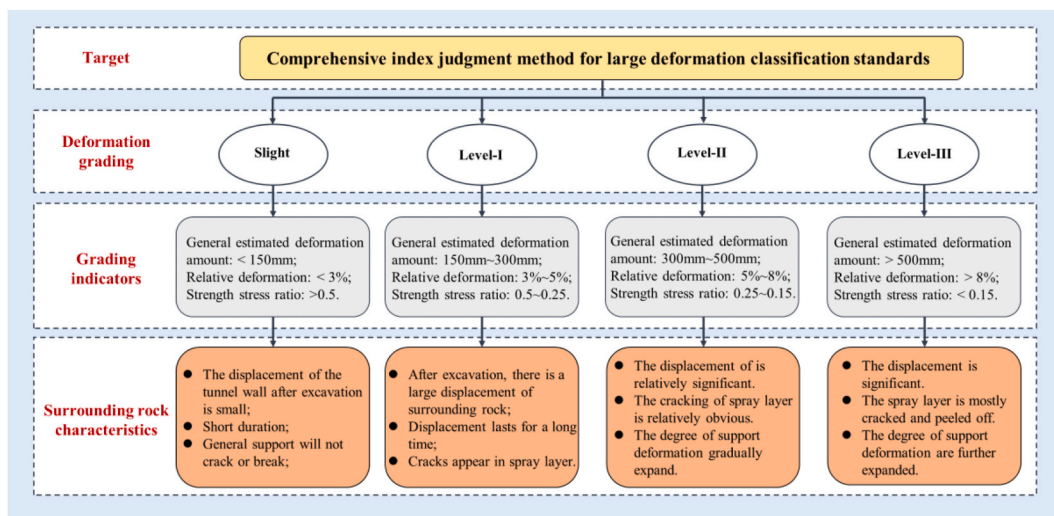

Fig. 7. Comprehensive index judgment method for large deformation classification standards.

Author contribution statement

Kai Cui: Conceived and designed the experiments; Performed the experiments; Wrote the paper.
Zheng Yang: Analyzed and interpreted the data; Contributed reagents, materials, analysis tools or data; Wrote the paper.

Data availability statement

Data will be made available on request.

Additional information

No additional information is available for this paper.

Declaration of competing interest

The authors declare that they have no known competing financial interests or personal relationships that could have appeared to influence the work reported in this paper.

References

[1] R. Peng, Y. Ju, J.G. Wang, H. Xie, F. Gao, L. Mao, Energy dissipation and release during coal failure under conventional triaxial compression, Rock Mech. Rock Eng. 48 (2) (2015) 509–526.
[2] C.-P. Lu, G.-J. Liu, Y. Liu, N. Zhang, J.-H. Xue, L. Zhang, Microseismic multi-parameter characteristics of rockburst hazard induced by hard roof fall and high stress concentration, Int. J. Rock Mech. Min. Sci. 76 (2015) 18–32.
[3] M.C. He, J.L. Miao, J.L. Feng, Rock burst process of limestone and its acoustic emission characteristics under true-triaxial unloading conditions, Int. J. Rock Mech. Min. Sci. 47 (2) (2010) 286–298.
[4] Z. Yang, T. Yin, D. Zhuang, Y. Wu, J. Yin, Y. Chen, Effect of temperature on mixed mode I/III fracture behavior of diorite: an experimental investigation, Theor. Appl. Fract. Mech. 122 (2022), 103571.
[5] T. Yin, Z. Yang, Y. Wu, X. Tan, M. Li, Experimental investigation on the effect of open fire on the tensile properties and damage evolution behavior of granite, Int. J. Damage Mech. 31 (8) (2022) 1139–1164.
[6] L.J. Dong, Q.M. Luo, Investigations and new insights on earthquake mechanics from fault slip experiments, Earth Sci. Rev. (2022) 228.
[7] L.J. Dong, Q.M. Luo, Stress Heterogeneity and Slip Weakening of Faults under Various Stress and Slip, GEOFLUIDS, 2020, p. 2020.
[8] Q. Zheng, Y. Xu, H. Hu, J. Qian, Y. Ma, X. Gao, Quantitative damage, fracture mechanism and velocity structure tomography of sandstone under uniaxial load based on acoustic emission monitoring technology, Construct. Build. Mater. 272 (2021), 121911.
[9] T. Xu, Y. Yuan, M.J. Heap, G.-L. Zhou, M.S.A. Perera, P.G. Ranjith, Microwave-assisted damage and fracturing of hard rocks and its implications for effective mineral resources recovery, Miner. Eng. 160 (2021), 106663.
[10] H. Gu, X. Lai, M. Tao, W. Cao, Z. Yang, The role of porosity in the dynamic disturbance resistance of water-saturated coal, Int. J. Rock Mech. Min. Sci. 166 (2023), 105388.
[11] Z. Yang, T. Yin, Y. Wu, D. Zhuang, J. Yin, J. Ma, Mixed-mode I/II fracture properties and failure characteristics of microwave-irradiated basalt: an experimental study, Fatig. Fract. Eng. Mater. Struct. 46 (3) (2023) 814–834.
[12] B. Haimson, C. Chang, A new true triaxial cell for testing mechanical properties of rock, and its use to determine rock strength and deformability of Westerly granite, Int. J. Rock Mech. Min. Sci. 37 (1–2) (2000) 285–296.
[13] C. Chang, B. Haimson, True triaxial strength and deformability of the German Continental Deep Drilling Program (KTB) deep hole amphibolite, J. Geophys. Res. Solid Earth 105 (B8) (2000) 18999–19013.
[14] X.G. Zhao, J. Wang, M. Cai, C. Cheng, L.K. Ma, R. Su, et al., Influence of unloading rate on the strainburst characteristics of beishan granite under true-triaxial unloading conditions, Rock Mech. Rock Eng. 47 (2) (2014) 467–483.
[15] Q.M. Gong, L.J. Yin, S.Y. Wu, J. Zhao, Y. Ting, Rock burst and slabbing failure and its influence on TBM excavation at headrace tunnels in Jinping II hydropower station, Eng. Geol. 124 (2012) 98–108.
[16] D.Y. Sun, Y.F. Wu, L.J. Dong, Q.M. Luo, Closed-form solutions for locating heat-concentrated sources using temperature difference, Mathematics 10 (16) (2022).
[17] J. Liu, P. Cao, D. Han, Sequential indentation tests to investigate the influence of confining stress on rock breakage by tunnel boring machine cutter in a biaxial state, Rock Mech. Rock Eng. 49 (4) (2016) 1479–1495.
[18] Q. Jiang, M. Zhang, F. Yan, G. Su, X. Feng, D. Xu, et al., Effect of initial minimum principal stress and unloading rate on the spalling and rockburst of marble: a true triaxial experiment investigation, Bull. Eng. Geol. Environ. 80 (2) (2021) 1617–1634.
[19] H. Zhao, M. Tao, X. Li, H. Mikada, S. Xu, Influence of excavation damaged zone on the dynamic response of circular cavity subjected to transient stress wave, Int. J. Rock Mech. Min. Sci. 142 (2021), 104708.
[20] H. Zhao, M. Tao, X. Li, W. Cao, C. Wu, Estimation of spalling strength of sandstone under different pre-confining pressure by experiment and numerical simulation, Int. J. Impact Eng. 133 (2019), 103359.
[21] Y. Chen, J. Zuo, Z. Li, R. Dou, Experimental investigation on the crack propagation behaviors of sandstone under different loading and unloading conditions, Int. J. Rock Mech. Min. Sci. 130 (2020), 104310.

[22] T. Backers, S. Stanchits, G. Dresen, Tensile fracture propagation and acoustic emission activity in sandstone: the effect of loading rate, Int. J. Rock Mech. Min. Sci. 42 (7) (2005) 1094–1101.

[23] J. Šílený, A. Milev, Seismic moment tensor resolution on a local scale: simulated rockburst and mine-induced seismic events in the kopanang gold mine, South Africa, Pure Appl. Geophys. 163 (8) (2006) 1495–1513.

[24] G-a Zhu, L-m Dou, C-b Wang, Z-w Ding, Z-j Feng, F. Xue, Experimental study of rock burst in coal samples under overstress and true-triaxial unloading through passive velocity tomography, Saf. Sci. 117 (2019) 388–403.

[25] N.W. Xu, T.B. Li, F. Dai, R. Zhang, C.A. Tang, L.X. Tang, Microseismic monitoring of strainburst activities in deep tunnels at the jinping II hydropower station, China, Rock Mech. Rock Eng. 49 (3) (2016) 981–1000.

[26] X.-T. Feng, H. Xu, S.-L. Qiu, S.-J. Li, C.-X. Yang, H.-S. Guo, et al., In situ observation of rock spalling in the deep tunnels of the China jinping underground laboratory (2400 m depth), Rock Mech. Rock Eng. 51 (4) (2018) 1193–1213.

[27] B.C. Haimson, F.H. Cornet, ISRM Suggested Methods for rock stress estimation—Part 3: hydraulic fracturing (HF) and/or hydraulic testing of pre-existing fractures (HTPF), Int. J. Rock Mech. Min. Sci. 40 (7) (2003) 1011–1020.

[28] J.A. Wang, H.D. Park, Comprehensive prediction of rockburst based on analysis of strain energy in rocks, Tunn. Undergr. Space Technol. 16 (1) (2001) 49–57.

[29] C.Q. Zhang, X.T. Feng, H. Zhou, S.L. Qiu, W.P. Wu, Case histories of four extremely intense rockbursts in deep tunnels, Rock Mech. Rock Eng. 45 (3) (2012) 275–288.

[30] Q. Jiang, X.-T. Feng, T.-B. Xiang, G.-S. Su, Rockburst characteristics and numerical simulation based on a new energy index: a case study of a tunnel at 2,500 m depth, Bull. Eng. Geol. Environ. 69 (3) (2010) 381–388.

[31] Y. Yang, D. Zhang, S. Li, L. Yang, L. Jin, In-situ stress test and rockburst analysis in Micang Mountain tunnel, Energy Sources, Part A Recovery, Util. Environ. Eff. 44 (1) (2022) 2321–2330.

[32] B. Russenes, Analysis of Rock Spalling for Tunnels in Steep Valley Sides, Norwegian Institute of Technology, 1974.

[33] Q. Jia, L. Wu, B. Li, C. Chen, Y. Peng, The comprehensive prediction model of rockburst tendency in tunnel based on optimized unascertained measure theory, Geotech. Geol. Eng. 37 (4) (2019) 3399–3411.

[34] J. Yang, W. Chen, X. Tan, D. Yang, Analytical estimation of stress distribution in interbedded layers and its implication to rockburst in strong layer, Tunn. Undergr. Space Technol. 81 (2018) 289–295.

[35] I.A. Turchaninov, G.A. Markov, Conditions of changing of extra-hard rock into weak rock under the influence of tectonic stresses of massifs, in: ISRM International Symposium, 1981. ISRM-IS-1981-090.